Original scientific paper

MULTI-OBJECTIVE OPTIMIZATION AND PERFORMANCE ANALYSIS OF BIMORPH MAGNETO-ELECTRO-ELASTIC ENERGY HARVESTERS

Meisam Moory Shirbani, Sayed Ehsan Alavi

Faculty of Engineering, Shohadaye Hoveizeh Campus of Technology,
Shahid Chamran University of Ahvaz, Dashte Azadegan, Iran

Abstract. *This study thoroughly investigates the multi-objective optimization of a magneto-electro-elastic (MEE) harvester in bimorph configurations and by the new method of Harris Hawk's optimization (HHO). The harvesters are configured in both series and parallel connections and under harmonic excitation to explore the effects of various parameters on the performance of the harvesting system. The primary objective is to maximize the total harvested power. Optimization involves various parameters, including dimensions, relative displacement changes, voltage, and current values. The Pareto fronts from the HHO method reveal optimal points in different configurations and scenarios. Notably, the optimal points are selected based on the criterion of maximum total power. The results reveal distinct optimal points for each objective function, demonstrating trade-offs between performance metrics. These findings provide valuable insights into the design and operation of efficient energy harvesters in MEE systems. The parallel configuration outperforms the series connection in terms of the current generation. Moreover, the evaluation of the overall performance of the energy harvesters in terms of total harvested power indicated that both series and parallel connections could lead to promising outcomes. However, the series connection exhibited a more dominant effect on maximizing the total harvested power, proving its relevance in pursuing the highest possible power output.*

Key words: *Multi-objective optimization, MEE harvester, Harris Hawk's optimization (HHO), Series and parallel connections*

1. INTRODUCTION

Energy harvesting involves converting environmental sources such as wind, heat, and vibrations into electrical energy. Mechanical vibrations are present in almost every

industrial device as a reliable energy source. Energy harvesting from ambient vibrations has gained substantial popularity due to its accessibility in various places and times [1-3].

This field involves multiple aspects of engineering disciplines, including mechanics, materials science, and electronics. Smart materials that can couple at least two fields, such as piezoelectric materials [4-6], MEE materials [7,8], and others [9,10], are employed in this energy conversion process. The potential applications of this technology were extensive, with one of its most efficient domains being wireless sensor networks. Piezoelectric energy harvesters have been used, often as cantilever beams and usually made of two layers [11-13]. Among notable initial works, the design and fabrication of a generator by Roundy et al. [14] in 2003 is noteworthy. This generator can produce 375 μW of power per 1 cm^3 with a density of 5.8 mW/gcm^3, sufficient output power for many low-power microelectronic devices.

Among the most significant works conducted in the analytical and numerical modeling of energy harvesting from piezoelectric materials, the contributions of Erturk and Inman are noteworthy [15,16]. They delved into the analytical modeling of piezoelectric energy harvesters by considering electrical and mechanical parameters, subsequently comparing and validating their results with experimental data. Utilizing a simple cantilever beam structure and operating in a frequency range of 450 Hz, they successfully achieved a power density of 6.8 mW/gcm^3. Researchers are employing various techniques, such as changing the type of piezoelectric material, altering electrode patterns, and layering energy harvesters to enhance the harvested power [17,18].

The MEE composites exhibit sensitivity to a magnetic field in addition to their sensitivity to an electric field [19-21]. With these dual sensitivities, these materials can interconvert mechanical, electrical, and magnetic energies, positioning them as superior and more versatile than piezoelectric materials. In 2018, Shirbani et al. [22] proposed using MEE composites in energy harvesters to enhance the electrical power density. They provided analytical modeling of the coupled mechanical, electrical, and magnetic dynamic responses of the suggested energy harvesters. An important outcome of their work was the positive impact of the new structure and circuit design used for the external coils around the composite layers, resulting in a 43% increase in the total harvested power. They also explored the influence of temperature differences between the different layers of MEE energy harvesters [23].

The optimization technique holds significant importance in mechanics, as it strives to discover the most optimal solutions to intricate problems while weighing various constraints and objectives [24-26]. Mechanics employ optimization techniques to design and analyze structures, systems, and processes that can efficiently withstand forces, stresses, and dynamic conditions. Optimization algorithms help engineers find the best configuration or parameters that lead to better performance, lower costs, and better safety. This paper aims to provide a comprehensive overview of the bimorph MEE energy harvester research, mainly focusing on applying multi-objective optimization using the HHO method. The optimization process involves the simultaneous consideration of various objective functions, enabling the identification of optimal solutions that balance competing design criteria. Multi-objective optimization offers a holistic approach to achieving the highest levels of efficiency and performance, catering to different operational scenarios and requirements.

The HHO is a relatively recent optimization algorithm inspired by the hunting behavior of Harris's hawks [27], a type of raptor bird. The algorithm was proposed to solve complex

optimization problems by simulating the social hunting behaviors of these birds. HHO aims to balance exploration and exploitation, leveraging the collaborative behavior of hawks during hunting. The HHO algorithm was introduced in a research paper by Heidari et al. [27] in 2019. The algorithm was designed to address optimization problems by imitating the cooperative hunting strategies of Harris's hawks. The HHO algorithm has gained attention due to its unique optimization approach inspired by nature. However, like any optimization algorithm, its effectiveness depends on the problem and its characteristics. Researchers continue to explore its potential and refine its techniques for various applications [28,29].

2. ENERGY HARVESTER EQUATIONS AND OPTIMIZATION APPROACH

In the present work, energy harvesters are analyzed as cantilever beams under the assumptions of the Euler-Bernoulli beam theory, coupled with layers possessing active MEE properties. In this context, energy harvesting refers to the extraction of vibrational energy derived from the vibration of the base of the beam. With transverse vibration, the beam undergoes strain. As a result of electrical and magnetic polarization, an electric and magnetic potential difference is established along the polar axis of the beam, enabling the generation of electrical power. The beam features embedded electrically conductive electrodes (for utilizing the electric field generated and extracting electrical energy) with minimal thickness, spanning the entire beam length.

Additionally, external coils (for utilizing the induced magnetic field and extracting magnetic energy) are present. Other assumptions include the linear behavior of magnetic, electric, and elastomer properties concerning strain, electric, and magnetic fields. Figures 1a and 1b illustrate the analyzed configurations. These configurations feature symmetric arrangements with layer connections in series (Fig. 1a) and parallel (Fig. 1b). In Fig. 1, i_E, R_E, V_M, i_M, and R_M represent the voltage, current generated, and external electrical resistance across the electrodes and the voltage, induced current and external electrical resistance across the external coils. Furthermore, w_{bT} denotes the transverse base excitation. The fundamental equations that characterize mechanical, electrical, and magnetic behaviors of materials with active MEE properties are expressed as follows [22]:

$$\sigma_i = C_{ik}\varepsilon_k + e_{ik}E_k + f_{ik}H_k \tag{1a}$$

$$D_k = e_{ik}\varepsilon_i + h_{kj}E_j + g_{kj}H_j \tag{1b}$$

$$B_k = f_{ik}\varepsilon_i + g_{kj}E_j + \mu_{kj}H_j \tag{1c}$$

In these equations, σ_i, D_i, and B_i represent the stress tensor, electric displacement, and magnetic flux density. Also, C_{ij}, h_{ij}, and μ_{ij} denote the tensor of elastic stiffness, and electric and magnetic permeability coefficients, respectively. The distinguishing feature of this class of materials from piezoelectric materials lies in the simultaneous influence of the strain fields ε_k, electric field E_k, and magnetic field H_k on stress, electric displacement, and magnetic flux density, characterized by the piezoelectric coefficients e_{ij}, piezomagnetic coefficients f_{ij}, and magnetoelectric coefficients g_{ij}. The strain component along the beam ε_1 according to the relative displacement w_{rel} is expressed as:

$$\varepsilon_1 = -z \frac{\partial^2 w_{rel}(x,t)}{\partial x^2} = -z w_{rel,xx} \qquad (2)$$
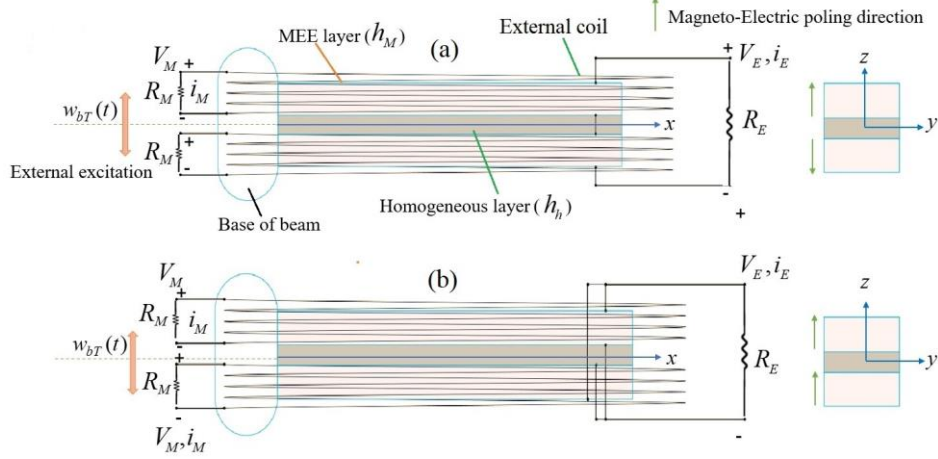

Fig. 1 Symmetric configurations of the MEE energy harvester; (a) Series connection, (b) Parallel connection of harvester layers

2.1 Equations Governing Mechanical Motion Coupling for Bimorph MEE Energy Harvesters

In this section, the Euler-Bernoulli cantilever beam with the configurations depicted in Fig. 1 is considered the energy harvester. By applying a base excitation in the transverse direction w_{bT}, the overall displacement change of each point along the beam $w(x,t)$ is as follows:

$$w(x,t) = w_{bT}(t) + w_{rel}(x,t) \qquad (3)$$

The governing differential equation for the forced vibrations of the Euler-Bernoulli cantilever beam under base excitation is expressed by Eq. (4) [7]:

$$\frac{\partial^2 M(x,t)}{\partial x^2} + c_m \frac{\partial w_{rel}(x,t)}{\partial t} + m \frac{\partial^2 w_{rel}(x,t)}{\partial t^2} = -[m]\frac{\partial^2 w_{bT}(x,t)}{\partial t^2} \qquad (4)$$

The bending moment $M(x,t)$ is the area moment of inertia, c_m is the damping coefficient, m is the mass per unit length L, and t is the time. The structural equations for expressing the coupling relationship in the MEE layers (denoted by the superscript M) in the axial direction using Eqs. (5a) to (5c), are presented as follows:

$$\sigma_1^M = C_{11}^M \varepsilon_1^M - e_{31}^M E_3^M - f_{31}^M H_3^M \qquad (5a)$$

$$D_3^M = e_{31}^M \varepsilon_1^M + h_{33}^M E_3^M + g_{33}^M H_3^M \qquad (5b)$$

$$B_3^M = f_{31}^M \varepsilon_1^M + g_{33}^M E_3^M + \mu_{33}^M H_3^M \qquad (5c)$$

Also, the stress-strain constitutive equation for the sublayer with homogeneous properties (marked with superscript h) is expressed as follows:

$$\sigma_1^h = C_{11}^h \varepsilon_1^h \tag{6}$$

It should be noted that based on the polarities indicated in Fig. 1, for the series connection (denoted by the superscript s), the electric field E_3 in both upper and lower layers is the same. For the parallel connection (denoted by the superscript p), the electric fields E_3 in both the upper and lower layers are equal in magnitude but opposite in direction [7].

$$E_3^s(t) = -V_E^s \Big/ 2h_M \, , 0.5h_h \leq z \leq h_M + 0.5h_h, -h_M - 0.5h_h \leq z \leq -0.5h_h \tag{7a}$$

$$\begin{cases} E_3^p(t) = -V_E^p \Big/ 2h_M \, , 0.5h_h \leq z \leq h_M + 0.5h_h \\[2mm] E_3^p(t) = +V_E^p \Big/ 2h_M \, , -h_M - 0.5h_h \leq z \leq -0.5h_h \end{cases} \tag{7b}$$

Furthermore, the magnetic field H_3 generated in the MEE layers is calculated using the induced voltage across the terminal of the external wire coils V_M and Ampere's law, along with the number of wire coil turns N, as given by Eq. (8) [7]:

$$H_3(t) = \frac{N i_M(t)}{h_M} = \frac{N V_M(t)}{R_M h_M} \tag{8}$$

The bending moments for each connection are calculated and expressed using the structural equations, electric and magnetic fields, and Euler-Bernoulli assumptions:

$$M(x,t) = \underbrace{EI_{eq} \frac{\partial^2 w_{rel}(x,t)}{\partial x^2}}_{M_{elas}(x,t)} + \underbrace{\Theta_{EM} V_E(t)[H(x) - H(x-L)]}_{M_{elec}(x,t)} + \underbrace{\Theta_{MM} V_M(t)[H(x) - H(x-L)]}_{M_{mag}(x,t)} \tag{9}$$

where M_{elas}, M_{elec}, and M_{mag} are the components of the bending moments that comprise elastic, electric, and magnetic components. The electric-mechanical and magnetic-mechanical coupling coefficients Θ_{EM} and Θ_{MM} are calculated for each connection.

$$\Theta_{EM}^p = 2\Theta_{EM}^s = b e_{31}^M (h_M + h_h) \tag{10a}$$

$$\Theta_{MM}^p = \Theta_{MM}^s = \frac{N f_{31}^M}{R_M} b(h_M + h_h) \tag{10b}$$

The equivalent flexural rigidity of the composite section EI_{eq} and mass per unit length are calculated for the bimorph configuration.

$$EI_{eq}^{\,s,p} = \frac{C_{11}^h b}{12}(h_h)^3 + \frac{C_{11}^M b}{3}\Big[(h_M + 0.5h_h)^3 - (0.5h_h)^3\Big] \tag{11a}$$

$$m^{s,p} = b(2\rho_M h_M + \rho_h h_h) \tag{11b}$$

The densities of the MEE and homogeneous layers are represented by ρ_M and ρ_h. Furthermore, b, h_M, and h_h represent the beam's width, the MEE layer's thickness, and the homogeneous layer's thickness, respectively. The derived motion equations can be solved using traditional modal analysis methods. By using variable separation techniques, the displacement variation of each point on the beam with respect to its base can be expressed through Eq. 12 [15]:

$$w_{rel}(x,t) = \sum_{r=0}^{\infty} W_r(x)T_r(t) \tag{12}$$

The time response of the beam and the shape of the r-th mode one-dimensional vibration of the cantilever beam are determined by $T_r(t)$ and $W_r(x)$. The coupled mechanical equations of motion in modal coordinates are derived after substituting Eq. (12) into Eq. (9) and then applying the orthogonality conditions of the mode shapes.

$$\frac{d^2T_r(t)}{dt^2} + 2\zeta_r\omega_r\frac{dT_r(t)}{dt} + \omega_r^2 T_r(t) + \alpha_{EMr}V_E(t) + \alpha_{MMr}V_M(t) = F_r(t) \tag{13}$$

The modal electric-mechanical and magnetic-mechanical coupling coefficients α_{EMr}, α_{MMr} are defined here and are calculated for each connection as follows:

$$\alpha_{EMr}^p = 2\alpha_{EMr}^s = be_{31}^M(h_M + h_h)\left[\frac{dW_r(x)}{dx}\right]_{x=L} \tag{14a}$$

$$\alpha_{MMr}^p = \alpha_{MMr}^s = -\frac{f_{31}^M N}{R_M}b(h_M + h_h)\left[\frac{dW_r(x)}{dx}\right]_{x=L} \tag{14b}$$

The natural frequency of the r-th mode is calculated using Eq. (15) [7]:

$$\omega_r^2 = \beta_r^2\sqrt{\frac{EI_{eq}}{ml^4}} \tag{15}$$

The damping ratio ζ_r and the mechanical force function $F_r(t)$ in modal coordinates are also defined as follows:

$$\zeta_r = \frac{c_m}{2m\omega_r} \tag{16a}$$

$$F_r(t) = -m\frac{d^2w_{bT}(t)}{dt^2}\int_0^L W_r(x)dx \tag{16b}$$

2.2 Governing Electrical Coupling Equations of Electrodes in Bimorph MEE Energy Harvesters

The differential equation governing the electrical circuit involving the two electrodes around the MEE layers is extracted in this section. The two electrode terminals and the external wire coils are connected to external electrical resistances R_E and R_M to use the generated voltages V_E and V_M. The electric charge created at the two electrode terminals

$q_E(t)$ can be determined through Gauss's law, which stipulates that the electric charge equals the integral of the electric displacement D_3^M over the electrode surfaces A_e. Furthermore, the electric current $i_E(t)$ equals the time derivative of the electric charge produced [7].

$$i_E(t) = \frac{dq_E(t)}{dt} = \frac{d}{dt} \iint_{A_e} D_3^M(x,t) dA_e \tag{17}$$

Consequently, the following equation is obtained for each connection using Eqs. (5b) and (17) and applying Ohm's law ($V = RI$).

$$\gamma_{C_M} C_M \frac{dV_E(t)}{dt} + \frac{\gamma_{R_E}}{R_E} V_E(t) = \sum_{r=1}^{\infty} \vartheta_{MEr} \frac{dT_r(t)}{dt} + \chi_{ME} \frac{dV_M(t)}{dt} \tag{18}$$

This equation defines C_M, υ_{MEr}, and χ_{ME} as the internal capacitance, modal mechanical-electrical, and magnetic-electrical coupling coefficients of the MEE layers, respectively. In addition to these parameters, the constants γ_{CM} and γ_{RE} for each connection are obtained as follows:

$$C_M = \frac{h_{33}^M bL}{h_M} \tag{19a}$$

$$\vartheta_{MEr}^{s,p} = -0.5 e_{31}^M (h_M + h_h) b \left. \frac{dW_r(x)}{dx} \right|_{x=L} \tag{19b}$$

$$\vartheta_{MEr}^{s,p} = -0.5 e_{31}^M (h_M + h_h) b \left. \frac{dW_r(x)}{dx} \right|_{x=L} \tag{19c}$$

$$\gamma_{C_M}^{p} = 2\gamma_{C_M}^{s} = 1 \tag{19d}$$

$$\gamma_{R_E}^{p} = 2\gamma_{R_E}^{s} = 2 \tag{19e}$$

2.3 Governing Electrical Coupling Equations of External Coils in Bimorph MEE Energy Harvesters

During vibrational excitation, the relative motion between the MEE layers and the external wire coils causes a change in the magnetic flux passing through the coils, resulting in an electric voltage. For the present energy harvester beam, the induced voltage in the wire coils results from changes in the magnetic flux density B_3^M. Consequently, V_M can be expressed as follows [7]:

$$V_M(t) = \frac{d}{dt} \int_{A_i} B_3^M(x,t) dA \tag{20}$$

By substituting Eqs. (12) and (20) into Eq. (5c), the differential equation for the electrical coupling in the circuit of the two wire coils is obtained:

$$L_c \frac{dV_M(t)}{dt} + R_M V_M(t) = \sum_{r=1}^{\infty} \vartheta_{MMr} \frac{dT_r(t)}{dt} + \chi_{EM} \frac{dV_E(t)}{dt} \tag{21}$$

In these equations, L_c, v_{MMr}, and χ_{EM} represent the self-inductance coefficients of the wire coils, the modal mechanical-magnetic and electric-magnetic coupling coefficients, respectively. These coefficients are derived for each connection as follows:

$$L_c = \mu_{33}^M N^2 \frac{bL}{h_M} \tag{22a}$$

$$\vartheta_{MEr}^{s,p} = -0.5 e_{31}^M (h_M + h_h) b \frac{dW_r(x)}{dx}\bigg|_{x=L} \tag{22b}$$

$$\chi_{ME}^{s,p} = \frac{g_{33}^M N}{R_M} \frac{bL}{h_M} \tag{22c}$$

2.4 Frequency Response of Bimorph MEE Energy Harvesters under Harmonic Base Excitation

The base excitation of the beam in the transverse direction at the excitation frequency ω is given as $w_{bT}(t) = W_{AT} e^{j\omega t}$, where W_{AT} represents the amplitude of the base transverse displacement. In this case, the expressions for the modal coordinates response of the beam, the voltages $V_E(t)$ and $V_M(t)$ are assumed as follows:

$$T_r(t) = T_{Ar} e^{j\omega t}, \quad V_E(t) = V_{AE} e^{j\omega t}, \quad V_M(t) = V_{AM} e^{j\omega t} \tag{23}$$

where T_{Ar}, V_{AE}, and V_{AM} represent the amplitudes of the modal coordinate response of the beam, the voltage across the two electrodes, and the voltage across the external coils, respectively. Also, the modal mechanical force function is rewritten as follows:

$$F_r(t) = F_{Ar} e^{j\omega t} = -m\omega^2 W_{AT} \int_0^L W_r(x)dx \left(e^{j\omega t}\right) \tag{24}$$

By substituting Eq. (23) into Eqs. (13), (18), and (21), the following expressions for $V_E(t)$, $V_M(t)$, and $w_{rel}(x,t)$ are obtained:

$$V_E(t) = \frac{\sum_{r=1}^{\infty} \frac{j\omega \vartheta_{MEr} F_{Ar}}{\left[(\omega_r^2 - \omega^2) + j(2\zeta_r \omega_r \omega)\right]} e^{j\omega t}}{\left[\left(\frac{1}{\gamma_{R_E} R_E} + \gamma_{C_M} j\omega C_M\right) + \sum_{r=1}^{\infty} \frac{j\omega \vartheta_{MEr} \alpha_{EMr}}{\left[(\omega_r^2 - \omega^2) + j(2\zeta_r \omega_r \omega)\right]}\right] + n_{ME}\left[\sum_{r=1}^{\infty} \frac{j\omega \vartheta_{MEr} \alpha_{MMr}}{\left[(\omega_r^2 - \omega^2) + j(2\zeta_r \omega_r \omega)\right]} - \chi_{ME}\right]} \tag{25}$$

$$V_M(t) = \frac{\sum_{r=1}^{\infty} \frac{j\omega \vartheta_{MMr} F_{Ar}}{\left[(\omega_r^2 - \omega^2) + j(2\zeta_r \omega_r \omega)\right]} e^{j\omega t}}{\left[(R_M + j\omega L_c) + \sum_{r=1}^{\infty} \frac{j\omega \vartheta_{MMr} \alpha_{MMr}}{\left[(\omega_r^2 - \omega^2) + j(2\zeta_r \omega_r \omega)\right]}\right] + n_{EM}\left[\sum_{r=1}^{\infty} \frac{j\omega \vartheta_{MMr} \alpha_{EMr}}{\left[(\omega_r^2 - \omega^2) + j(2\zeta_r \omega_r \omega)\right]} - \chi_{EM}\right]} \tag{26}$$

$$w_{rel}(x,t) = W_r(x) \frac{(R_2 + j\omega L_c)V_M(t) - \chi_{EM}V_E(t)}{j\omega \vartheta_r^{MM}} \tag{27}$$

where the parameters n_{ME} and n_{EM} represent the ratios of $V_M(t)$ to $V_E(t)$ and vice versa, respectively, have been obtained as follows:

$$n_{ME} = \frac{1}{n_{EM}} = \frac{V_M}{V_E} = \frac{\left[f_{31}^M NR_M (\frac{1}{\gamma_{R_E} R_E} + \gamma_{C_M} j\omega C_M) - j\omega(e_{31}^M \chi_{EM}) \right]}{\left[j\omega(f_{31}^M NR_M \chi_{ME}) - e_{31}^M (R_M + j\omega L_c) \right]} \tag{28}$$

Finally, by having the expressions for $V_E(t)$ and $V_M(t)$, the analytical relationships for the harvested electrical power $P_E(t)$, the harvested magnetic power $P_M(t)$, and the total harvested magneto-electric power $P_{ME}(t)$ by the MEE energy harvesting beam can be obtained. These equations provide a quantitative understanding of the energy harvesting performance of the MEE beam. They can be used to optimize their design and operation for various applications in wireless sensor networks and biomedical implants.

$$P_E(t) = \frac{V_E(t)^2}{2R_E} \tag{29}$$

$$P_M(t) = \frac{V_M(t)^2}{2R_M} \tag{30}$$

$$P_{ME}(t) = P_E(t) + P_M(t) \tag{31}$$

2.5 Multi-objective Optimization of Bimorph MEE Harvesters by New Method of HHO Algorithm

Optimization techniques are mathematical tools used to find the best solution for a given problem within a set of constraints. These techniques are widely used in various domains, such as engineering, economics, biology, and artificial intelligence. They help solve complex problems by finding the optimal solution that maximizes or minimizes a specific objective function. Optimization techniques have become increasingly popular in industries and academia due to their ability to provide efficient and effective solutions to problems.

One such innovative approach is the HHO algorithm, a population-based method inspired by the hunting behavior of Harris's hawks. It can be used for various optimization problems by utilizing appropriate formulas. The HHO simulates the behaviors of Harris's hawks in hunting scenarios to optimize solutions. The algorithm involves exploration and exploitation stages based on the prey's energy levels. Different strategies are modeled to mimic the prey's escape patterns and the Hawk's pursuit behaviors [27]. The principles of the HHO algorithm are summarized and illustrated in Fig. 2.
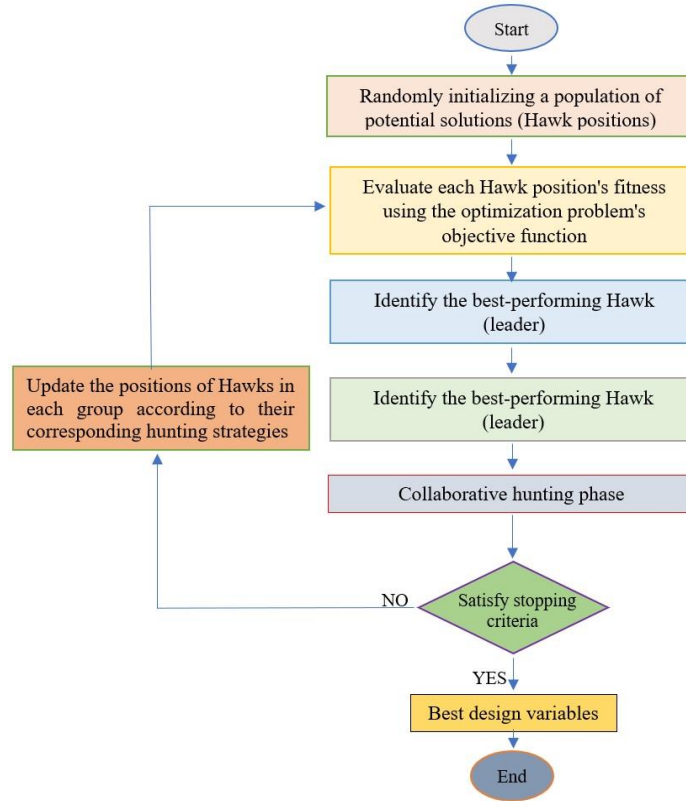
Fig. 2 Flowchart of the HHO algorithm for the determination of the best design variables

In the following, the bimorph MEE harvesters have been optimized using the novel algorithm of HHO and multi-objective optimizations. Five different multi-objective optimization cases, as introduced in the chart displayed in Fig. 3, are specified on the plots to determine the best performance of the energy harvesting device.
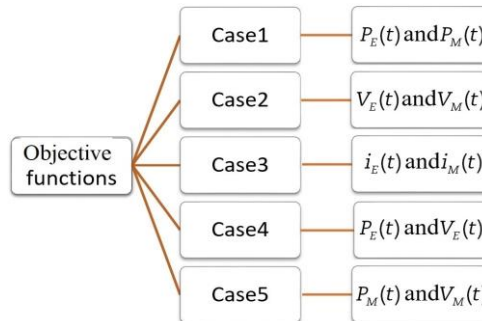

Fig. 3 Five different multi-objective cases and corresponding functions optimized by the HHO method

Also, the geometric and electrical design variables and their limits in terms of optimization are listed as follows:

$$l \le 100mm$$
$$b \le 10mm$$
$$h_h \ \& \ h_M \le 1mm \tag{32}$$
$$R_E \ \& \ R_M \le 10^6 \Omega$$
$$N \le 10$$

3. RESULTS AND DISCUSSION

This section presents the numerical results of the optimal connections for the series and parallel configurations of the energy harvesting beams. Table 1 provides the values of the properties of the harvesting layers. It should be noted that a composite material consisting of $BaTiO_3$-$CoFe_2O_4$ with a volumetric percentage of 50% is selected as the active layer, while aluminum is chosen as the homogenous layer. $BaTiO_3$-$CoFe_2O_4$ is a composite material with potential applications in energy harvesting due to its piezoelectric and magnetic properties.

Table 1 Properties of the MEE energy harvester layers

C_{11}^h (Nm^{-2})	75×10^9	g_{33} (NsV^{-1}C^{-1})	2600×10^{-12}
C_{11}^M (Nm^{-2})	225×10^9	μ_{33} (Ns^{2}C^{-2})	90×10^{-6}
e_{31} (Cm^{-2})	-3.5	ρ_h (kgm^{-3})	2707
f_{31} (NA^{-1})	350	ρ_M (kgm^{-3})	5550
h_{33} (C^{2}N^{-1}m^{-2})	6.3×10^{-9}	ζ	0.01

During the continuation of the analysis, the results of multi-objective optimization of the MEE energy harvester in series and parallel connections using the HHO algorithm were extracted and presented in Tables 2 and 3, which will help analyze the performance of the energy harvesting device and make informed decisions to optimize its efficiency. Also, as an example, in Figs. 4a and 4b, the multi-objective optimization results and the Pareto front for the first optimization case are shown. In these figures, points A, B, and C are optimal in this research phase.

The power of P_M is maximized for the series connection at point A, while the power of P_E is minimal. Neither of the two harvested powers is maximized at point B, but their values are in the desired optimal state. At point C, the power of P_E is maximized, while the power of P_M is almost minimized. Point C was selected as the optimal point based on the maximum total power P_{ME} criteria. In Fig. 4b, point A was selected for parallel connection as the result of optimization due to the maximum of both electrical powers. Other optimized variables have been obtained with another similar method and are listed in Tables 2 and 3.
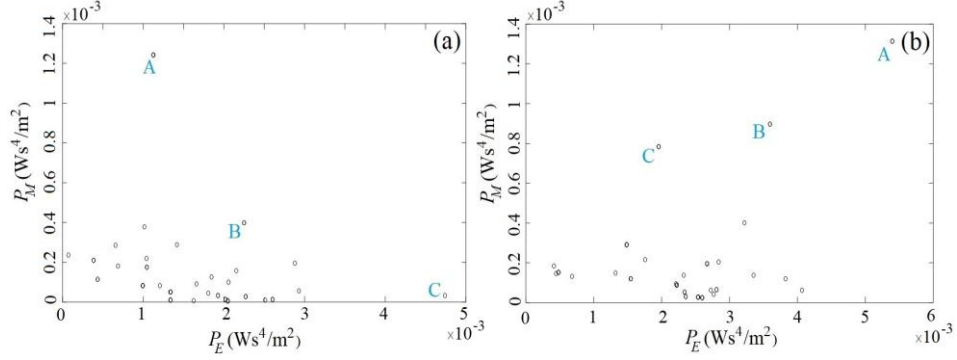
Fig. 4 Multi-objective optimization results and the Pareto front for the first case of optimization case; (a) Series connection, (b) Parallel connection

Table 2 Optimal multi-objective optimization variables for series connection

Series layers	R_E (Ω)	R_M (Ω)	N	h_M (mm)	h_h (mm)	L (mm)	b (mm)
Case1	107.992	0.008733	6	0.143	0.857	90.50	5.61
Case2	95.568	0.0156	10	0.122	0.878	92.72	8.80
Case3	126.744	0.0212	9	0.128	0.872	90.01	8.92
Case4	31681.40	876.35	7	0.112	0.888	89.12	8.63
Case5	34750.10	51.48	4	0.143	0.857	98.81	9.91

Table 3 Optimal multi-objective optimization variables for parallel connection

Parallel layers	R_E (Ω)	R_M (Ω)	N	h_M (mm)	h_h (mm)	L (mm)	b (mm)
Case1	15940.02	18.17	5	0.102	0.898	89.74	8.61
Case2	95.568	0.0156	7	0.143	0.857	91.11	9.53
Case3	126.744	0.0212	8	0.104	0.896	95.04	10
Case4	10011.50	651.52	6	0.100	0.900	92.01	10
Case5	10020.31	10.13	8	0.100	0.900	96.41	6.91

After obtaining the values of the optimized variables with the help of Eq. (25), the frequency response of the voltage V_E generated by each energy harvesting beam connection is plotted against the dimensionless excitation frequency η, considering the vicinity of their respective first natural frequencies. The results are depicted in Fig. 5, where Fig. 5a corresponds to the series connection, and Fig. 5b corresponds to the parallel connection. The parameters of the electrical circuits of the two-terminal electrodes and external coils, as well as the geometric values of the harvesting beams, are selected based on the values obtained from Tables 1 and 2 to plot these results. These figures show that the maximum voltage V_E is generated near the first natural frequency of the beam harvester.

Considering Fig. 5a, the maximum value of V_E for the series connection in the second optimization case is measured as 0.808 Vs^2/m. This value is notably higher than the

minimum V_E generated in the third case, indicating that the second optimization case can create a significantly higher V_E. Similarly, Fig. 5b demonstrates that the maximum optimal value of V_E for the parallel connection in the second optimization case is measured as 0.5771 Vs^2/m. This configuration generates up to 44.67% higher voltage V_E compared to the minimum optimization case, which is the third one.

Furthermore, it is observed that the maximum voltage occurs for excitation ratios less than $\eta = 1$. The optimal excitation ratios for the series and parallel connections are measured as 0.99904 and 0.99944, respectively. This phenomenon implies that the electrical circuits connected to the energy harvesting beams increase the damping ratio of the beams. This excitation ratio is defined as the damping ratio of the harvesting beams in the presence of electrical coupling, denoted as η_{dam}. Utilizing the relation $\eta_{dam} = (1-\zeta_{Elec}^2)^{0.5}$, where ζ_{Elec} represents the electrical damping ratio of the harvesting beams, the values of ζ_{Elec} are determined as 0.044 and 0.033 for the series and parallel connections, respectively. The series connection, characterized by a lower electrical damping ratio, exhibits a higher maximum voltage V_E, indicating the advantageous utilization of coupled electrical circuits for this configuration.
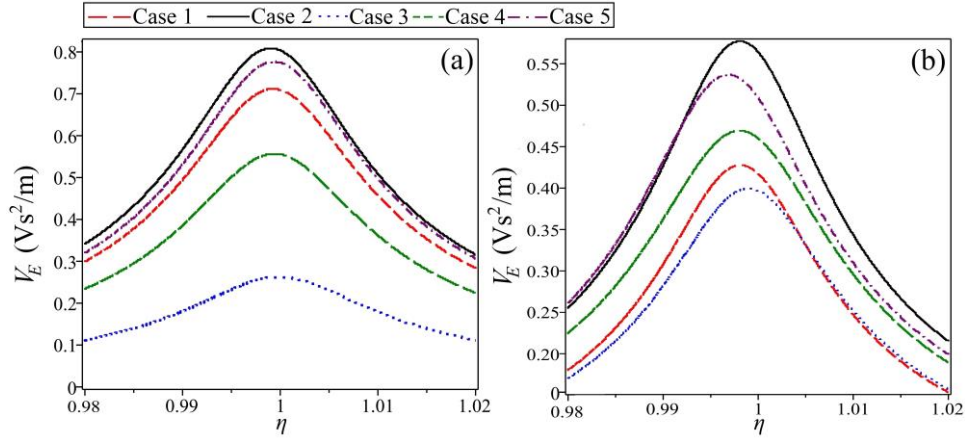

Fig. 5 Frequency response of the generated voltage V_E over the electrodes in five cases of optimization; (a) Series connection, (b) Parallel connection of bimorph MEE layers

By using Eq. (26), the frequency response of the voltage V_M is plotted for both the series (Fig. 6a) and the parallel connections (Fig. 6b). The maximum values of V_M are calculated as 0.025 Vs^2/m and 0.0212 Vs^2/m for the series and parallel connections, respectively. These values represent a 23% difference in the better performance of the series connection. Both of these maximum values occur in the third case. Furthermore, the maximum values of V_M are generated at the excitation ratios of 0.99986 and 0.99957 for the series and parallel connections, respectively. By utilizing the relation $\eta_{dam} = (1-\zeta_{Mag}^2)^{0.5}$ and the excitation ratios obtained from the results of Fig. 6, the magnetic damping ratio of the harvesting beams, ζ_{Mag}, can be determined. The values of ζ_{Mag} for the series and parallel connections are measured as 0.017 and 0.029, respectively. The series connection, characterized by a higher magnetic damping ratio, exhibits a lower maximum voltage V_M.

In the following, the frequency responses of currents i_E and i_M are obtained using Ohm's law and Eqs. (25) and (26). Then, the frequency response of i_E is plotted for both series and parallel connections in Figs. 7a and 7b, respectively. The optimal values of i_E are obtained for the series and parallel connections in the fifth and third optimization cases, respectively, as 22.321 μAs^2/m and 37.328 μAs^2/m. These values signify a 71.72% better parallel connection performance than the series connection. As a result, the parallel connection is essential for designing a new harvesting device with the highest possible amount of current, i_E.
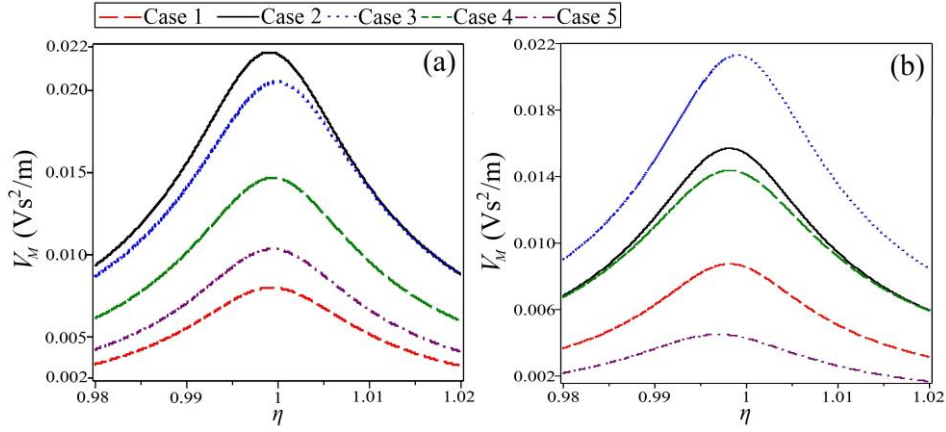

Fig. 6 Frequency response of the generated voltage V_M over the external coil in five cases of optimization; (a) Series connection, (b) Parallel connection of bimorph MEE layers
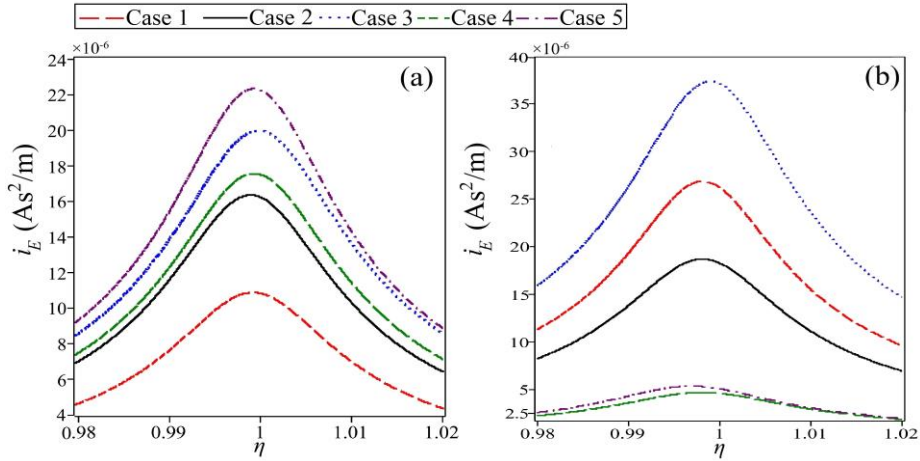

Fig. 7 Frequency response of the generated current i_E over the electrodes in five cases of optimization; (a) Series connection, (b) Parallel connection of bimorph MEE layers

According to Fig. 8a, the maximum value of i_M for the series connection in the fifth optimization case is 200.903 μAs²/m. This value indicates an increase of about 21.55 times compared to the first case. Also, Fig. 8b illustrates that the maximum amount of i_M in the parallel connection occurs in the first optimization case, measuring 480.71 μAs²/m. This value is 20.83 times higher than the minimum value in the fourth case. Also, the values obtained for the maximum values of i_M show that the parallel connection produces 1.39 times more electric current i_M.
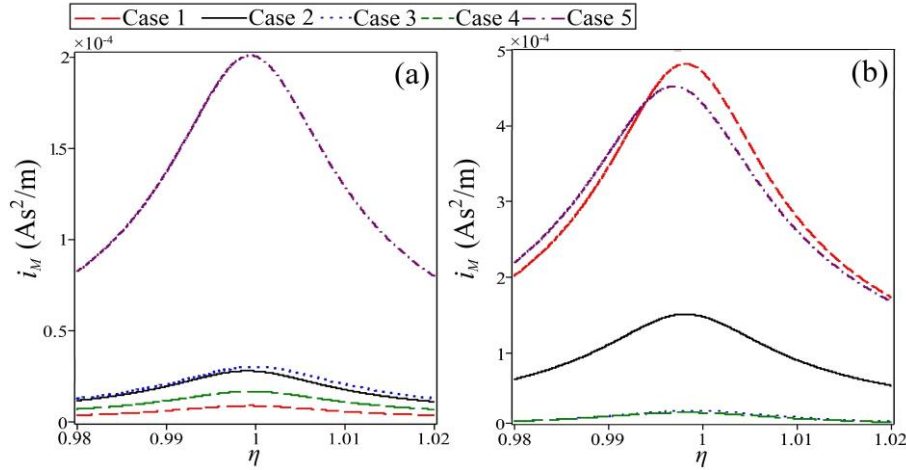

Fig. 8 Frequency response of the generated current i_M over the external coil in five cases of optimization; (a) Series connection, (b) Parallel connection of bimorph MEE layers

The comparison of different connection's performance examines how the arrangement of MEE layers, geometric dimensions, and electrical circuit parameters affect the harvested power by the electrodes P_E and external coils P_M. These results aid in selecting a more suitable and improved structure for these harvesters. The frequency response of P_E is plotted for both series and parallel connections in Figs. 9a and 9b. The optimal amount of P_E for the series connection occurs when the fifth optimization case is implemented. It has been observed that the maximum value of P_E will be attained in the third case for the parallel connection. The power values achieved are 8.66 μWs⁴/m² and 7.453 μWs⁴/m², respectively, indicating that the series connection produces around 16.19% more power P_E than the parallel connection. As a result, the series connection is preferred for achieving maximum generated power P_E.

The results related to the frequency response of the harvested power by the external coils P_M are extracted in the next step. The displayed results in Fig. 10a for the series connection still emphasize the significance of the fifth optimization case, which exhibits a remarkably more significant difference than other cases. This difference is so substantial that it indicates an 8.43 times difference with the fourth optimization case. The results for the parallel connection in Fig. 10b depict the superior performance of the first optimization case and a 77.07% difference with the second optimization case. The comparison between both connections demonstrates that the parallel connection performs better in generating 102.31% more harvested power P_M.
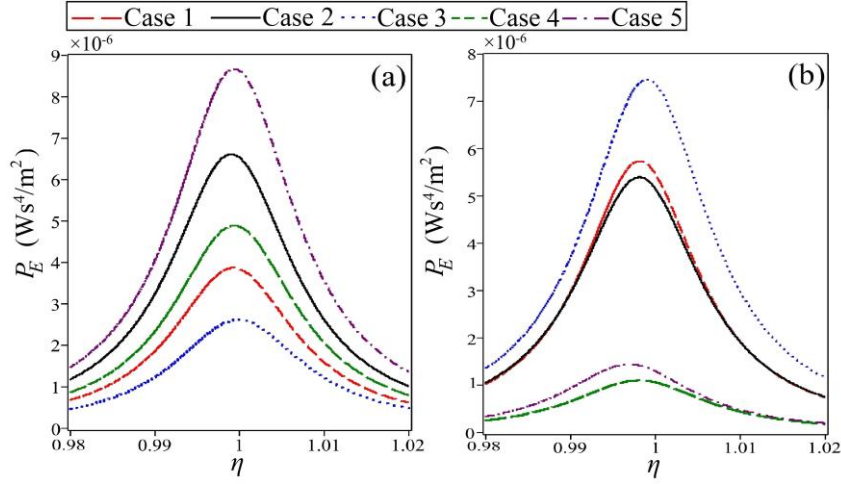
Fig. 9 Frequency response of the harvested power P_E by the electrodes in five cases of optimization; (a) Series connection, (b) Parallel connection of bimorph MEE layers

As mentioned, the ultimate goal in the design of harvesters is to achieve the maximum total harvested power. To this end, the total MEE harvested power P_{ME} results for both connections are depicted in Figs. 11a and 11b, respectively. The maximum values of P_{ME} have been measured for the series and parallel connections as 9.701 $\mu Ws^4/m^2$ and 7.833 $\mu Ws^4/m^2$, respectively. The highest value of P_{ME} in the series connection, achieved in the fifth optimization case, is 23.85% higher than the value obtained in the first case for the parallel connection. These results show the importance of series connection to achieve the highest total harvested power P_{ME}, which is the most crucial goal of a harvester.
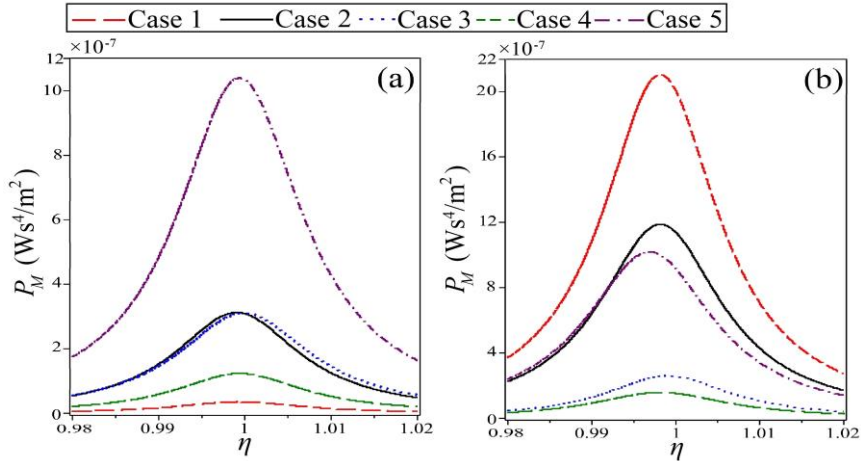

Fig.10 Frequency response of the harvested power P_M by the external coil in five cases of optimization; (a) Series connection, (b) Parallel connection of bimorph MEE layers
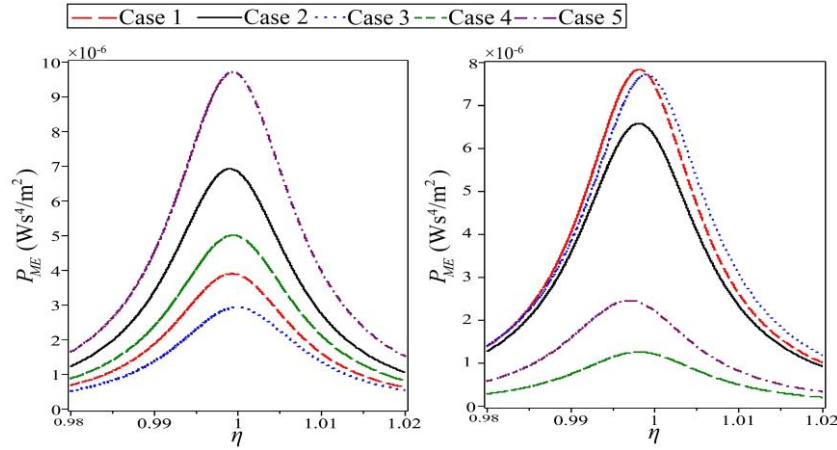
Fig. 11 Frequency response of the total MEE harvested power P_{ME} in five cases of optimization; (a) Series connection, (b) Parallel connection of bimorph MEE layers

In the final step, using Eq. (27), the tip relative displacement of the beam $w_{rel}(l)$ is calculated for both connections. The frequency responses of $w_{rel}(l)$ are then depicted in Figs. 12a and 12b, respectively. One of the reasons for examining this parameter is its fundamental role in the design of the harvester's volume. In other words, besides the dimensions of the beam, a specific range should be left empty for the beam's deflection so that the existing vibrations in the environment can be fully utilized. The results in Figs. 12a and 12b reveal that both connections exhibit similar maximum relative displacement changes in the fifth case. The maximum $w_{rel}(l)$ values for the series and parallel connections are 132.617 $\mu ms^2/m$ and 131.457 $\mu ms^2/m$, respectively. The choice of different objective functions in different optimization cases has led to 47.95% and 37.55% greater deflection $w_{rel}(l)$ in the series and parallel connections, respectively.
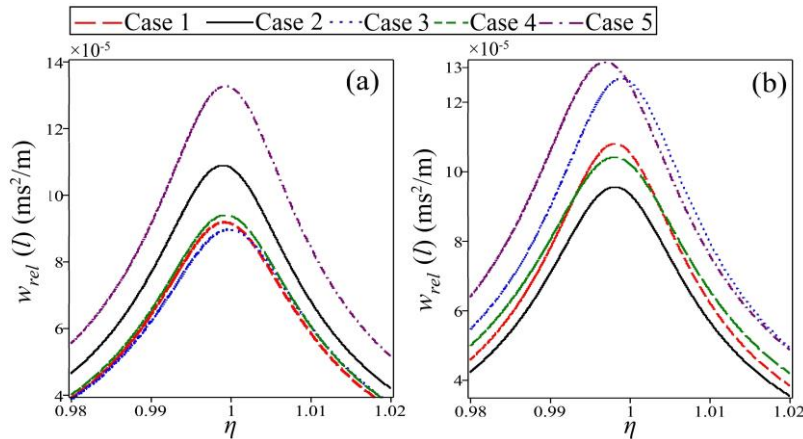

Fig. 12 Frequency response of the relative tip displacement $w_{rel}(l)$ in five cases of optimization; (a) Series connection, (b) Parallel connection of bimorph MEE layers

For a better comparison, the maximum values extracted from the plotted graphs in Tables 4 and 5 are provided for both connections, respectively. In the fifth optimization case, where the maximum power P_{ME} occurs, the contribution of P_E to the total power P_{ME} is 89.33% for the series connection. In this case, the optimal maximum value of the current i_M is 9.01 times the generated current, i_E. In the first optimization case of the parallel connection, the contribution of electrical power P_E to the maximum total harvested power P_{ME} is 73.16%, indicating a larger share of the circuit connected to the external coils in power generation compared to the series case. The optimal maximum value of i_M is 17.93 times the amount of the i_E, which is a significant amount for producing electrical current in a harvesting system.

Table 4 Optimal values of the objective functions in the series connection

Series layers	Case1	Case2	Case3	Case4	Case5
P_{ME} (μWs^4/m^2)	3.902	6.922	2.9258	5	9.701
P_E (μWs^4/m^2)	3.866	6.605	2.619	4.88	8.666
P_M (μWs^4/m^2)	0. 003561	0.0312	0.031	0.123	1.038
i_E (μAs^2/m)	10.874	16.354	19.967	17.56	22.321
i_M (μAs^2/m)	8.906	27.99	30.277	16.812	200.903
V_E (Vs^2/m)	0.7104	0.808	0.2622	0.5561	0.7759
V_M (Vs^2/m)	0.007978	0.0223	0.025	0.0146	0.0103
$Wrel$ (μms^2/m)	91.859	108.862	89.639	93.969	132.617

Table 5 Optimal values of the objective functions in the parallel connection

parallel layers	Case1	Case2	Case3	Case4	Case5
P_{ME} (μWs^4/m^2)	2.455	1.258	7.716	6.578	7.833
P_E (μWs^4/m^2)	1.436	1.099	7.453	5.392	5.731
P_M (μWs^4/m^2)	1.017	0.157	0.2606	1.186	2.1
i_E (μAs^2/m)	5.365	4.688	37.328	18.684	26.814
i_M (μAs^2/m)	451.033	22.024	24.489	151.318	480.71
V_E (Vs^2/m)	0.5367	0.4688	0.3989	0.5771	0.4273
V_M (Vs^2/m)	0.00431	0.0143	0.0212	0.0156	0.00873
$Wrel$ (μms^2/m)	131.457	104.142	126.744	95.568	107.992

4. CONCLUSIONS

This study comprehensively investigates the multi-objective optimization of a MEE energy harvester operating in both series and parallel connections. The main goal is to maximize the total harvested power by considering various objective functions, such as harvested power, voltage, and current. The study uses the HHO algorithm and looks at points on the Pareto fronts for each connection and objective function. The best candidate in each iteration is considered the target or a solution close to the optimum in the HHO algorithm. The algorithm randomly places hawks in different places based on specific identification strategies. The resulting equations describing the beam's mechanical displacement response, the harvested powers, voltages, and currents were formulated and presented according to the specified parameters. The frequency response of the bimorph configuration of the MEE energy harvesting system under harmonic excitation was

investigated after finding and using the optimal points. These findings provide valuable insights into the design and operation of efficient MEE energy harvesters. Specifically, the investigation emphasizes the importance of selecting the optimal point based on the criterion of maximum total power. The results show that each objective function has its optimal point, which shows how performance metrics are related. These findings provide valuable insights into the design and operation of efficient MEE energy harvesters. It is found that the parallel connection produces more electrical current than the series connection, while the series connection produces more harvested power. The impact of various parameters on the system's performance is discussed, highlighting the significance of optimizing the configuration and parameter selections.

REFERENCES

1. Wei, C., Jing, X., 2017, *A comprehensive review on vibration energy harvesting: modelling and realization*, Renewable and Sustainable Energy Reviews, 74, pp. 1-18.
2. Wang, J., Geng, L., Ding, L., Zhu, H., Yurchenko, D., 2020, *The state-of-the-art review on energy harvesting from flow-induced vibrations*, Applied Energy, 267, 11490.
3. Yang, T., Zhou, S., Fang, S., Qin, W., Inman, D.J., 2021, *Nonlinear vibration energy harvesting and vibration suppression technologies: designs, analysis, and applications*, Applied Physics Reviews, 8(3), 031317.
4. Safaei, M., Sodano, H.A., Anton, S.R., 2019, *A review of energy harvesting using piezoelectric materials: state-of-the-art a decade later (2008–2018)*, Smart Materials and Structures, 28(11), 113001.
5. Covaci, C., Gontean, A., 2020, *Piezoelectric energy harvesting solutions: A review*, Sensors, 20(12), 3512.
6. Milić P., Marinković D., Klinge S., Ćojbašić Ž., 2023, *Reissner-Mindlin Based Isogeometric Finite Element Formulation for Piezoelectric Active Laminated Shells*, Tehnicki Vjesnik, 30(2), pp. 416-425.
7. Shirbani, M.M., Shishesaz, M., Hajnayeb, A., Sedighi, H.M., 2018, *Design and analytical modeling of magneto-electro-mechanical characteristics of a novel magneto-electro-elastic vibration-based energy harvesting system*, Journal of Sound and Vibration, 425, pp. 149-169.
8. Siddharth Mangalasseri, A., Mahesh, V., Ponnusami, S.A., Harursampath, D., 2023, *Investigation on the interphase effects on the energy harvesting characteristics of three phase magneto-electro-elastic cantilever beam*, Mechanics of Advanced Materials and Structures, 30(13), pp. 2735-2747.
9. Xu, J., Tat, T., Zhao, X., Xiao, X., Zhou, Y., Yin, J., Chen, K., Chen, J., 2023, *Spherical magnetoelastic generator for multidirectional vibration energy harvesting*, ACS Nano, 17(4), pp. 3865-3872.
10. Soliman, M.S.M., Abdel-Rahman, E.M., El-Saadany, E.F., Mansour, R.R., 2008, *A wideband vibration-based energy harvester*, Journal of Micromechanics and Microengineering, 18(11), 115021.
11. Wu, Y., Qiu, J., Zhou, S., Ji, H., Chen, Y., Li, S., 2018, *A piezoelectric spring pendulum oscillator used for multidirectional and ultra-low frequency vibration energy harvesting*, Applied Energy, 231, pp. 600-614.
12. Wang, Z., Du, Y., Li, T., Yan, Z., Tan, T., 2021, *A flute-inspired broadband piezoelectric vibration energy harvesting device with mechanical intelligent design*, Applied Energy, 303, 117577.
13. Abdelkareem, M.A., Jing, X., Eldaly, A.B.M., Choy, Y., 2023, *3-DOF X-structured piezoelectric harvesters for multidirectional low-frequency vibration energy harvesting*, Mechanical Systems and Signal Processing, 200, 110616.
14. Roundy, S., Wright, P.K., Rabaey, J., 2003, *A study of low-level vibrations as a power source for wireless sensor nodes*, Computer Communications, 26(11), pp. 1131-1144.
15. De Marqui Júnior, C., Erturk, A., Inman, D.J., 2009, *Modelling and analysis of cantilevered piezoelectric energy harvesters*, In Proceedings of COBEM, pp. 41-77.
16. Erturk, A., Inman, D.J., 2009, *An experimentally validated bimorph cantilever model for piezoelectric energy harvesting from base excitations*, Smart Materials and Structures, 18(2), 025009.
17. Anton, S.R., Farinholt, K.M., Erturk, A., 2014, *Piezoelectric foam–based vibration energy harvesting*, Journal of Intelligent Material Systems and Structures, 25(14), pp. 1681-1692.
18. Zhang, Z., Lin, S., Gu, Y., Zhang, L., Wang, S., Zhai, S., Kan, J., 2023, *Design and characteristic analysis of a novel deformation-controllable piezoelectric vibration energy harvester for low frequency*, Energy Conversion and Management, 286, 117016.
19. Vinyas, M., 2021, *Computational analysis of smart magneto-electro-elastic materials and structures: review and classification*, Archives of Computational Methods in Engineering, 28(3), pp. 1205-1248.

20. Zaheri Abdehvand, M., Seyed Roknizadeh, S.A., Sedighi, H.M., 2021, *Parametric study of a novel magneto-electro-aeroelastic energy harvesting system*, Proceedings of the Institution of Mechanical Engineers, Part L: Journal of Materials: Design and Applications, 235(9), pp. 2100-2111.

21. Zhou, L., Qu, F., 2023, *The magneto-electro-elastic coupling isogeometric analysis method for the static and dynamic analysis of magneto-electro-elastic structures under thermal loading*, Composite Structures, 315, 116984.

22. Shirbani, M.M., Shishehsaz, M., 2023, *Modelling of a novel magneto-electro-elastic energy harvesting system subjected to applied electric voltage with simultaneous use as an electrical actuator system*, Iranian (Iranica) Journal of Energy and Environment, 14(2), pp. 168-176.

23. Alavi, S.E., Shirbani, M.M., Hassani, A.M., 2023, *Analytical investigation of the effect of temperature difference between layers of unimorph piezoelectric harvesters*, Iranian Journal of Science and Technology, Transactions of Mechanical Engineering, pp. 1-14.

24. Sarker, M.R., Julai, S., Sabri, M.F.M., Said, S.M., Islam, M.M., Tahir, M., 2019, *Review of piezoelectric energy harvesting system and application of optimization techniques to enhance the performance of the harvesting system*, Sensors and Actuators A: Physical, 300, 111634.

25. Mavrovouniotis, M., Li, C., Yang, S., 2017, *A survey of swarm intelligence for dynamic optimization: Algorithms and applications*, Swarm and Evolutionary Computation, 33, pp. 1-17.

26. Alavi, S.E., Shirbani, M.M., Tondro, M.K., 2023, *Exergy-economic optimization of gasket-plate heat exchangers*, Journal of Computational Applied Mechanics, 54(2), pp. 254-267.

27. Heidari, A.A., Mirjalili, S., Faris, H., Aljarah, I., Mafarja, M., Chen, H., 2019, *Harris hawk's optimization: Algorithm and applications*, Future Generation Computer Systems, 97, pp. 849-872.

28. Abbasi, A., Firouzi, B., Sendur, P., 2021, *On the application of Harris hawk's optimization (HHO) algorithm to the design of microchannel heat sinks*, Engineering with Computers, 37, pp. 1409-1428.

29. Dhawale, D., Kamboj, V.K., Anand, P., 2023, *Optimum generation scheduling incorporating wind energy using HHO–IGWO algorithm*, Journal of Electrical Systems and Information Technology, 10, 1.